IEEE Access
Multidisciplinary | Rapid Review | Open Access Journal

Received 13 November 2023, accepted 26 November 2023, date of publication 28 November 2023,
date of current version 5 December 2023.

Digital Object Identifier 10.1109/ACCESS.2023.3337355

RESEARCH ARTICLE

Capacity Analysis of Full-Duplex Directional Wireless Mobile Networks

AYMAN T. ABUSABAH, (Member, IEEE), AND RODOLFO OLIVEIRA, (Senior Member, IEEE)
Departamento de Engenharia Electrotécnica e de Computadores, Faculdade de Ciências e Tecnologia (FCT), Universidade Nova de Lisboa, 2829-516 Caparica, Portugal
Instituto de Telecomunicações, 1049-001 Lisbon, Portugal

Corresponding author: Rodolfo Oliveira (rado@fct.unl.pt)

This work was supported by the Fundação para a Ciência e Tecnologia through the projects CELL-LESS6G under Grant 2022.08786.PTDC and Grant UIDB/50008/2020.

ABSTRACT This paper presents a comprehensive study of capacity characterization in mobile wireless networks employing directive communications and full-duplex communication technology. We address the impact of nodes' mobility, directive beams, and full-duplex capabilities on the network capacity. Firstly, we derive the signal-to-interference-plus-noise ratio (SINR) for a reference receiver, considering the combined effects of mobility, directive beams, and full-duplex communications. The derived SINR is then utilized to calculate the network's capacity. To validate the proposed model, extensive simulations are performed, incorporating various scenarios of mobility levels, self-interference suppression levels in the full-duplex wireless system, and different receiving thresholds. The simulation results confirm the accuracy and effectiveness of the derived SINR-based capacity characterization model under real-world conditions. Furthermore, we study the probability of a receiver simultaneously decoding multiple packets as a function of the receiver's threshold and full-duplex self-interference suppression. The probability is crucial for assessing the network performance and facilitating future optimization schemes aimed at regulating the number of competing nodes in a given spatial region. The validated model and probability characterization offer valuable insights into network performance evaluation and can be instrumental in devising future efficient optimization strategies for managing network contention at the medium access control and enhancing the network performance.

INDEX TERMS Mobile wireless networks, ad hoc networks, in-band full-duplex radio systems, directive communications, performance analysis.

I. INTRODUCTION

The growing demand for high data rates and reliable wireless communication has led to intensive research on capacity characterization in modern wireless networks [1], [2], [3], [4], [5], [6]. Directional wireless communications and in-band full-duplex (IBFDX) cancellation schemes have emerged as promising solutions to enhance spectral efficiency and system performance. Directional communication networks [7], [8], involve transmitting signals through highly focused directional beams instead of traditional omnidirectional transmissions. Directional communications effectively increase the signal gain and reduce interference, enabling higher spatial reuse and improved capacity. Several approaches have been proposed to model and optimize the use of directive communications, such as beamforming algorithms [9], adaptive array techniques [10], and beam tracking methods [11].

IBFDX communication schemes [12] allow nodes to simultaneously transmit and receive data over the same frequency band, having the potential of increasing spectral efficiency [13]. However, IBFDX creates self-interference challenges that must be mitigated to achieve satisfactory performance. Research in IBFDX has focused on self-interference cancellation techniques, including analog and/or digital cancellation methods [14], [15], [16], adaptive cancellation algorithms [17], and modeling of the self-interference due to inefficient cancellation of the self-transmitted signal at the receiving radio frequency (RF) chain [18], [19].

The associate editor coordinating the review of this manuscript and approving it for publication was Wei Feng.

The integration of directional communications with IBFDX is a promising avenue to further enhance wireless capacity. This combination enables high-directional gains for both transmission and reception, effectively reducing interference and self-interference, as identified in [20] and [21]. The coexistence of directional communications and IBFDX introduces complex challenges, such as beam misalignment, interference management, and self-interference suppression, which are currently being addressed and proposed as a promising solution for future cellular networks [22].

Capacity characterization of directional wireless networks with IBFDX requires careful consideration of various parameters, including mobility, spatial distribution of nodes, and interference conditions. The work in [20] evaluated IBFDX communications in a cellular scenario, where a base station simultaneously transmits to one device while receiving from another. The authors consider the case where the base station can use directional antennas to explore the spatial diversity and increase the passive level of suppression to achieve higher IBFDX cancellation, comparing its performance gain to an omnidirectional antenna scenario. In the same direction, the study presented in [21] investigated the impact of directional antennas on the reduction of multiuser interference and self-interference (SI) in an uplink cellular network scenario, showing that the adoption of directional communications achieves significant performance gains.

In the literature, analytical models and system-level simulations have been employed to evaluate the achievable capacity in directional IBFDX networks, such as in [20], [21], [23], and [24]. In [23], the authors evaluate the impact of directional antennas on the interference mitigation of IBFDX cellular networks. The work considers the case when the user and the base station implement IBFDX communications (two-node architecture) and the case when only the base station implements IBFDX while the users operate in half-duplex mode (three-node architecture), showing that the three-node architecture performance can be increased with the employment of more directional antennas, while the performance to the two-node architecture is degraded for that scenario. However, the proposed model relies on approximate assumptions of angular passive SI suppression (for the three-node architecture) and exponential residual SI, and no nodes' mobility is considered. The work in [24] introduces several contributions to the characterization of the transport capacity of IBFDX directional ad hoc networks. The work derived both upper and lower bounds for the network transport capacity, showing that IBFDX can approximately double the transport capacity when compared to a half-duplex scenario. However, [24] is only considering the average SI power on the derivation of the transport capacity, and no nodes' mobility is considered, as in [23].

While significant progress has been made in capacity characterization for directional IBFDX networks, several challenges remain. These challenges motivate this paper and include the impact of realistic self-interference conditions, dynamic mobility scenarios, and more realistic modeling of directional communications. In this paper, we investigate the capacity of IBFDX directional networks. When compared to the works in [23] and [24], the innovative aspects of our approach rely on the assumption of nodes' mobility and more realistic self-interference and directional beamforming models. The contributions of this paper as summarized as follows:

- Nodes' mobility is considered in a multi-transmitter to a single-receiver scenario, which can be adopted in both cellular or ad hoc network scenarios. Mobility introduces time-varying channel conditions and beam misalignment, causing different levels of interference to the receiver, and influence the overall network capacity;
- We consider more realistic models for IBFDX and directional beam patterns. The distribution of the residual SI power in an IBFDX scheme follows the model derived in [19], which can be parametrized for different SI channels and SI cancelation errors. A directional beamforming model representing a sectored antenna with M-beams is generic enough to consider low-power beams that influence the aggregate interference at the receiver;
- The aggregate interference caused to a receiver operating in full-duplex mode is accurately approximated by a generalized extreme value (GEV) distribution. A closed-form solution of the parameters of the GEV distribution is provided, which takes into account the spatial distribution of the nodes and their mobility, the properties of the directional beam pattern, and the SI cancellation process. Several simulations validate the high accuracy of the aggregate interference model;
- Assuming that multiple transmitters can communicate with a single receiver, we derive the approximate number of successfully received packets for a given signal-to-interference-plus-noise ratio (SINR) threshold, which is accurately validated by simulations;
- Finally, we characterize the distribution of a receiver simultaneously decoding multiple packets as a function of the receiver's threshold and full-duplex SI suppression. The characterization offers valuable insights into devising future efficient optimization strategies for managing network contention at the medium access control and enhancing the network performance.

The rest of the paper is organized as follows: Section II presents the network scenario assumed in the paper, as well as the IBFDX model, the beamforming model, and the multipacket capture condition at the receiver. Section III characterizes the capacity of the receiver by deriving the distribution of the SINR as a function of the network mobility, IBFDX parameterization, and antenna beams' properties. Section III also includes an approximation for the expected number of successfully received packets at the receiver. The validation of the proposed model as well as its analysis is presented in Section IV. Finally, the conclusion of the paper is given in Section V.

Notation: $\mathbb{P}[X = x]$ denotes the probability of a random variable (RV) X. The functions $f_X(.)$ and $F_X(.)$ represent

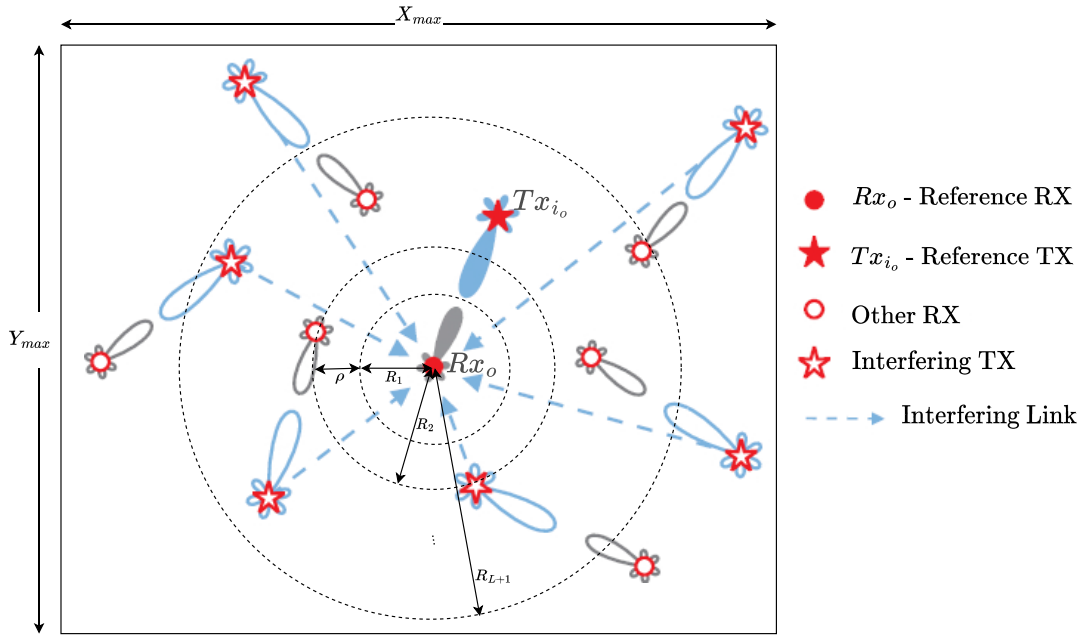

FIGURE 1. A reference node Rx_o acts as a receiver (RX) and receives information from the reference transmitter (TX) node Tx_{i_o}. Simultaneously, n moving transmitters ("Interfering TX") with directional beamforming capability cause interference to the reference node Rx_o. The inner circle radius is denoted by R_1 while R_{L+1} denotes the outer circle radius.

the probability density function (PDF) and the cumulative density function (CDF), respectively. E[X] denotes the expectation of the RX X. $M_X(s) = \mathrm{E}[e^{sX}] = \int_{-\infty}^{\infty} e^{sx} f_X(x)\,dx$ represents the moment generating function (MGF) of the RV X, where $\mu_n^X = \mathrm{E}[X^n] = \frac{d^n}{ds^n} M_X(s)|_{s=0}$ is the n-th raw-moment of the RV X. Gamma(k, θ) is the Gamma distribution, where k and θ represent the shape and scale parameters, respectively. The Gamma function and the incomplete gamma function are given by $\Gamma(x)$ and $\Gamma(p, x)$, respectively. ${}_2\mathrm{F}_1(a, b; c; z)$ represents the Gauss Hypergeometric function. Finally, the symbols adopted in this work are listed in Table 1.

II. SYSTEM MODEL AND ASSUMPTIONS

A. NETWORK MODEL

We assume that $(n+1)$ nodes are distributed over a rectangular region $X_{max} \times Y_{max}$ as shown in Fig. 1. The nodes are moving according to the random waypoint (RWP) model described in [25]. Initially, one of the nodes is randomly selected to act as a transmitter, Tx_{i_o}, communicating with a reference receiver, Rx_o, located at position (x_o, y_o), $x_o \in [0, X_{max}]$ and $y_o \in [0, Y_{max}]$. The remaining n nodes act as interferers to the intended link between Tx_{i_o} and Rx_o.

According to the RWP model, the location of each node (x, y) is randomly chosen from the uniform distribution in such $x \in [0, X_{max}]$ and $y \in [0, Y_{max}]$. Due to the mobility, the nodes move with velocity v to a new position that is also uniformly selected. The velocity v is uniformly sampled from $v \in [V_{min}, V_{max}]$. The nodes remain stopped for a pause time T_p and then repeat the same cycle. Consequently, the average velocity of each node is given by [25]

$$\mathrm{E}[V] = \frac{\mathrm{E}[S]}{(\mathrm{E}[V_{wp}])^{-1}\mathrm{E}[S] + T_p}, \tag{1}$$

where $\mathrm{E}[V_{wp}] = \left(\frac{V_{max} - V_{min}}{\ln(\frac{V_{max}}{V_{min}})}\right)$ represents the average velocity of the nodes when the pause time approaches zero and E[S] denotes the average distance between the positions of any two randomly selected nodes.

We use the spatial circular model (SCM) proposed in [26] and [27] and depicted in Fig. 1 to compute the received SINR at a reference node Rx_o. The SCM admits L annuli where the width of each annulus $l \in \{1, \ldots, L\}$ is represented by ρ. Therefore, the radii of the outer and inner circumferences of the annulus l are given by $R_{l+1} = (R_1 + l\rho)$ and R_l, respectively. Regarding the circular area where the nodes are located, it is simply a composition of a finite number L of annuli areas $A = \sum_{l=1}^{L} A_l$, where $A_l = \pi\left((R_{l+1})^2 - (R_l)^2\right)$ represents the area of the annulus l.

The RV X_l represents the number of nodes located within a specific annulus l which can be approximated by a Poisson process [28], being its truncated probability mass function (PMF) given by [29]

$$P(X_l = k) = \frac{\frac{(\lambda_l A_l \tau_a)^k}{k!} e^{-\lambda_l A_l \tau_a}}{\sum_{i=0}^{n} \frac{(\lambda_l A_l \tau_a)^i}{i!} e^{-\lambda_l A_l \tau_a}}, \quad k = 0, 1, \cdots, n, \tag{2}$$

where λ_l denotes the nodes' spatial density for the l-th annulus, n represents the number of the nodes distributed over

TABLE 1. Table to symbols adopted in this work.

Symbol	Definition
A_l	Area of the annulus l
α	Propagation loss coefficient
b	Capture threshold
BW	Bandwidth
E_{RX}	Mean of received packets
ϵ	Residual channel gain estimation
f_c	Carrier frequency
$\mathcal{F}$	Noise figure
g	Directivity gain
$g_t(\theta_t)$	Gain of the transmitting node
$g_r(\theta_r)$	Gain of the receiving node
g_i	Directional gain
g_i	Directional gain
γ_i	SINR
h	Residual channel gain
I_{agg}	Aggregate Interference Power
I_l	Interference power caused in annulus l
I_i	Interference power caused in node i
k_o, θ_o	Wireless channel parameters
l	$l-$th annulus
L	Number of annuli
λ_l	Node´s spatial density
M	Number of transmitter beams
n	Number of network nodes
$\mathcal{N}$	Noise power
N_s	RV - number of received packets
$P^r_{i_o}$	Received power at Rx_o
$P_{y_{res}}$	Residual self-interference power
P_l	Probability that a node is within annulus l
P_{Succ}	Prob. of successfully reception
ϕ	Residual channel phase error
r_i	Distance - transmitter to receiver
Rx_o	Receiver node
ρ	Annulus width
S	RV - Distance between 2 nodes
σ^2_N	Noise variance
σ^2_N	Noise variance
Tx_{i_o}	Transmitter node
τ	Residual channel delay
τ_a	Nodes' channel access probability
v, V	Velocity of the nodes
X_{max}, Y_{max}	Coordinates of the mobility region
X_l	RV - Number of nodes in annulus l
Y	Interference plus noise
ω_c	Angular carrier frequency
Z^l_a	RV - node within the annulus l

the network, and τ_a represents the channel access probability depending on the adopted MAC protocol and/or policies, such as the preamble transmission probability in an MTC or mURLLC network. We highlight that the RWP mobility model causes inhomogeneity in the spatial distribution of the nodes.

Assuming that $f_{X,Y}(x, y)$ is the PDF representing the nodes' motion in x-y plane as described in [27, eq. (4)], then, the probability that a moving node is located within the annulus l is written as follows

$$\begin{aligned} P_l &= P(Z^l_a = 1) \\ &= \int_{(x_o-R_{l+1})}^{(x_o+R_{l+1})} \int_{\left(y_o-\sqrt{(R_{l+1})^2-(x-x_o)^2}\right)}^{\left(y_o+\sqrt{(R_{l+1})^2-(x-x_o)^2}\right)} f_{XY}(x, y)\, dy\, dx \\ &\quad - \int_{(x_o-R_l)}^{(x_o+R_l)} \int_{\left(y_o-\sqrt{(R_l)^2-(x-x_o)^2}\right)}^{\left(y_o+\sqrt{(R_l)^2-(x-x_o)^2}\right)} f_{XY}(x, y)\, dy\, dx, \end{aligned} \tag{3}$$

where Z^l_a is a Bernoulli RV representing the hypothetical presence of a node within the l-th annulus. Therefore, the nodes' spatial distribution is approximated by an IPP where λ_l takes different values for each annulus l as follows [27]

$$\lambda_l = \frac{nP_l}{A_l}. \tag{4}$$

Using the Riemann sum, the area A can be partitioned into a finite number L of small annuli areas that together form the interference region being measured. Therefore, the inhomogeneity of the nodes' density across the whole area A can be approximated through multiple homogeneous Poisson processes (L) over each partitioned area A_l with a specific corresponding density (λ_l). This methodology has been validated in [27] considering different mobility scenarios. We highlight that the accuracy of the approximation depends mainly on the parameterization of L.

B. SINR MODEL

We denote the received SINR at reference node Rx_o by γ_i, given as follows

$$\gamma_i = \frac{P^r_{i_o}}{Y}, \tag{5}$$

where $P^r_{i_o}$ is the intended received power at Rx_o due to the transmission of Tx_{i_o} node. Note that, the Tx_{i_o} is selected independently and randomly from the set of the $n+1$ transmitters. $Y = I_{agg} + P_{y_{res}} + \mathcal{N}$, where I_{agg} represents the aggregate interference power generated by the n nodes in the interference region. $P_{y_{res}}$ is the residual self-interference power resulting from the adoption of IBFDX radio at the reference receiver node Rx_o. The noise is assumed to be independent and identically distributed drawn from a zero-mean normal distribution with variance (σ^2_N). Therefore, the noise power, $\mathcal{N}$, can be represented by a chi-squared distribution with 1 degree of freedom as follows $\mathcal{N} \sim \sigma^2_N \chi^2_1$. By definition, if $\sigma^2_N > 0$, then, $\mathcal{N} \sim \sigma^2_N \chi^2_1 \sim \text{Gamma}\left(\frac{1}{2}, 2\sigma^2_N\right)$. The variance is defined as $\sigma^2_N(\text{dBm}) = -174 + 10\log_{10}(\text{BW}) + \mathcal{F}$, where $\sigma^2_N = \frac{10^{\sigma^2_N(\text{dBm})/10}}{10^3}$, $\mathcal{F}$ represents the noise figure, BW denotes the total utilized bandwidth, and 174 dBm/Hz is the reference noise level at room temperature.

The aggregate interference caused by the interfering links can be seen as the sum of interference generated by nodes

located within each annulus with area A_l as follows

$$I_{agg} = \sum_{l=1}^{L} I_l. \tag{6}$$

Assuming that n_l nodes are bounded by the annulus l such that $\sum_{l=1}^{L} n_l = n$, then, I_l is the interference power seen at the reference node Rx_o from the interferers bounded by the annulus l, which is given by

$$I_l = \sum_{i=1}^{n_l} I_i, \tag{7}$$

where I_i is the received signal power from the i-th interfering node.

C. IBFDX RADIO MODEL

It is well-known that the practical implementation of the cancellation schemes in full-duplex in-band radios introduces undesirable residual self-interference [30]. Mainly, the gain and phase estimation errors of the SI channel, in addition to the hardware impairments at the transmitter and receiver sides, turn the total elimination of the self-interference into a challenging task. Therefore, the characterization of the residual SI is crucial to design efficient estimation and cancellation schemes.

Fig. 2 represents the block diagram of an IBFDX analog canceler, where $\omega_c = 2\pi f_c$ represents the angular carrier frequency, and $x(t)$ is the SI signal. The fading channel is described through the delay, τ, and the channel gain, h. In order to minimize the residual SI signal, y_{res}, the channel parameters are estimated, $\hat{\tau}$ and $\hat{h}$, and compensated in the cancellation loop. The estimated gain is given by $\hat{h} = \epsilon h$ where $(1-\epsilon)$ is the gain estimation error, $0 \le \epsilon \le 1$. The phase estimation error is given by $\phi = \omega_c(\tau - \hat{\tau})$.

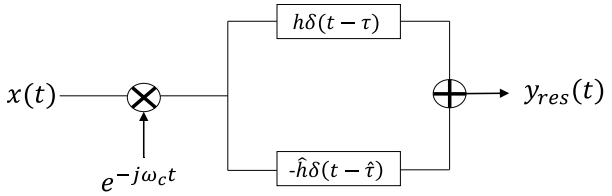

FIGURE 2. IBFDX radio model.

The power of the residual SI signal, $P_{y_{res}}$, after the analog cancellation, has been theoretically characterized for different SI channels. In particular, for Rician SI channels, the distribution of the residual SI power is given by [19]

$$f_{P_{y_{res}}}(z) \approx \frac{2^{\frac{1-k}{2}} \sigma_x^{-k-1} \theta^{-k}}{\Gamma(k)} \times (\theta/z)^{\frac{k-1}{2}} z^{k-1} K_{(k-1)}\left(\sqrt{\frac{2z}{\sigma_x^2 \theta}}\right), \tag{8}$$

where

$$k = \frac{(\nu^2 + 2\sigma^2)^2}{4\sigma^2(\nu^2 + \sigma^2)}, \quad \theta = \frac{4\sigma^2(\nu^2 + \sigma^2)C}{(\nu^2 + 2\sigma^2)^2}, \tag{9}$$

in which $\nu^2 = \frac{K\Omega}{1+K}$ and $\sigma^2 = \frac{\Omega}{2(1+K)}$ where K and Ω are the Rician channel parameters. The notation $K_{(k-1)}(.)$ represents the modified Bessel function of the second kind. The parameter K represents the ratio between the LoS power component and the non-LoS power components, and Ω denotes the total power from both components. The SI signal, $x(t)$, is a circularly symmetric complex signal drawn from normal distributions with zero mean and σ_x standard deviation. The parameter $C = \left(1 + \epsilon^2 - 2\epsilon\cos(\phi)\right)$ is a constant representing the power of estimation errors [19]. The condition $C = 0$ occurs when the channel gain and phase are perfectly estimated, i.e., $\epsilon = 1, \phi = 0$, leading to a null residual SI.

D. COMMUNICATION MODEL

We attribute the variations in the envelope of the received signal power to both large-scale fading and small-scale fading, given as follows

$$I_i = P_i^t h_i g_i r_i^{-\alpha}, \tag{10}$$

where P_i^t represents the power of the transmitted signal, h_i denotes the fading channel gain between the i-th node and the reference receiver. The notation $g_i = g_t(\theta_t) g_r(\theta_r)$ denotes the total directivity gain in the i-th node to the Rx_o node, where $g_t(\theta_t)$ is the gain of the transmitting node and $g_r(\theta_r)$ is the gain of the receiving node, while θ_t and θ_r are the boresight angle directions of the transmitting and receiving antennas, respectively. The parameter $r_i > 1$ is the distance to Rx_o from the i-th node, and $\alpha > 2$ is the propagation loss coefficient. We highlight that h_i, g_i, and r_i represent instant values of the RVs H_i, G_i and R_i, respectively.

E. CHANNEL MODEL

We adopt the Gamma distribution to approximate the power of the fading channel, which is a valid approximation when there is no line-of-sight (LoS), as in the Rayleigh fading channel or the LoS link as in the Rician fading channel [31]. Therefore, for a gamma-distributed channel, we obtain

$$H_i \sim \text{Gamma}\,(k_o, \theta_o)\,. \tag{11}$$

Given that the distribution of the nodes is homogeneous within each annulus l over $A_l = \pi\left((R_{l+1})^2 - (R_l)^2\right)$, then, the PDF of the distance to the node Rx_o, represented by the RV R_i, is given by

$$f_{R_i}(r) = \frac{2r}{(R_{l+1})^2 - (R_l)^2}, \quad R_l \le r \le R_{l+1}. \tag{12}$$

Consequently, the PDF of $Q_l = R_i^{-\alpha}$ is found as follows

$$f_{Q_l}(q) = -\frac{2q^{\frac{-2}{\alpha}-1}}{\alpha\left((R_{l+1})^2 - (R_l)^2\right)}, \ (R_{l+1})^{-\alpha} \le q \le (R_l)^{-\alpha}. \tag{13}$$

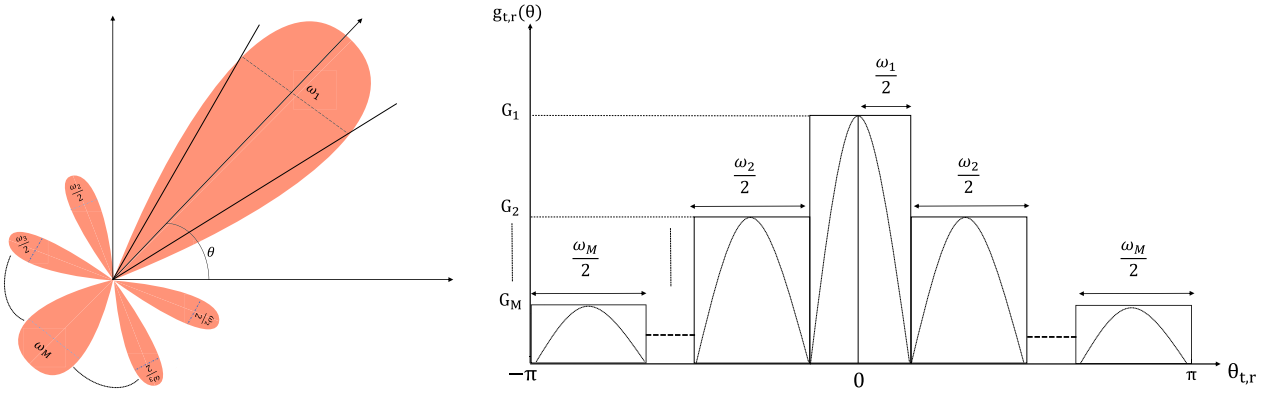

FIGURE 3. Multi-Beams sectored antenna model.

F. BEAMFORMING MODEL

We assume that all nodes are equipped with antenna arrays to perform directional beamforming. We adopt a sectored antenna model with M-beams (one main-lobe and $M-1$ back-lobes) as shown in Fig. 3, to represent the gain patterns $g_t(\theta_t)$ and $g_r(\theta_r)$ as follows

$$g_{t,r}(\theta_{t,r}) = \begin{cases} G_1, \left(\dfrac{-\omega_1}{2} \le \theta_{t,r} \le \dfrac{\omega_1}{2}\right) \\ G_m, \left(-\dfrac{1}{2}\displaystyle\sum_{j=1}^{m}\omega_j \le \theta_{t,r} \le -\dfrac{1}{2}\sum_{j=1}^{m-1}\omega_j\right) \text{ or} \\ \left(\dfrac{1}{2}\displaystyle\sum_{j=1}^{m-1}\omega_j \le \theta_{t,r} \le \dfrac{1}{2}\sum_{j=1}^{m}\omega_j\right) \\ G_M, \left(-\pi \le \theta_{t,r} \le -\dfrac{1}{2}\displaystyle\sum_{j=1}^{m}\omega_j\right) \text{ or} \\ \left(\dfrac{1}{2}\displaystyle\sum_{j=1}^{m}\omega_j \le \theta_{t,r} \le \pi\right). \end{cases} \tag{14}$$

While 1-sidelobe pattern approximation has been used as an initial model of the radiation gain and was adopted in several works [32], [33], [34], [35], it does not represent a realistic array pattern where the gain changes over the angular position. This is mainly because the power of the sidelobes is continuously descending in nature. With the 1-sidelobe pattern approximation adopted in [32], [33], [34], and [35], the authors have clearly assumed two levels of power, the main lobe power radiated over its main beamwidth and the sidelobe power radiated over the rest of the angular space. While the second sidelobe power level is relatively small to the peak of the main beam and the first sidelobe, the resulting cumulative interference cannot be ignored in the case of high-density scenarios of distributed nodes where the aggregation of the small power values can effectively degrade the performance. By considering the 1-sidelobe pattern, the captured/sensed interference could be greater than its real value since it is not descending over the angular space. Therefore, we introduce a multi-sidelobes pattern that is more realistic as it considers a higher decaying level of the sidelobes over the angular space.

To obtain a more realistic beam pattern, the proposed beamforming model adopts multi-level of gains $\{G_1, \ldots, G_M\}$, with $G_1 > G_2 > \ldots > G_M$, defined by corresponding beamwidths $\{\omega_1, \ldots, \omega_M\}$ in which $\left(\sum_{j=1}^{M} = \omega_j = 2\pi\right)$, and the boresight angle direction $\theta_{t,r} \in [-\pi, \pi)$.

Without loss of generality, all nodes are assumed to be on the same horizontal plane and the beam pattern does not variate over the elevation angle. The orientation of the beams of each node is sampled from the uniform distribution in $[-\pi, \pi)$. According to (14), the gain distributions, $g_t(\theta_t)$ or $g_r(\theta_r)$, are discrete and their PMF is given by

$$f_{G_{t,r}}(g) = \sum_{j=1}^{M} p_i \delta(g - G_j), \tag{15}$$

where $p_i = \omega_i/2\pi$ in which $\sum_{i=1}^{M} p_i = 1$.

The directivity gain, G_i, is merely a product between the two random gains G_t and G_r, in which the PMF of each one is given by (15). Thus, the PMF of G_i is formulated as follows

$$f_{G_i}(g) = \sum_{j=1}^{M} p_j^2 \delta(g - G_j^2) + \sum_{j=1,k=1,j\neq k}^{M} p_j p_k \delta(g - G_j G_k) \tag{16}$$

G. MULTIPACKET CAPTURE CONDITION

The receiver can decode packets from multiple transmitters. The performance of the multipacket receiver (MPR) is measured by the capture condition ($\gamma_i > b$) [36], where b is the capture threshold that specifies the receiver's sensitivity. The condition $b > 1$ represents Single-Packet Reception (SPR) receivers, while $b < 1$ represents receivers with MPR capability [37]. Consequently, the MPR reception occurs whenever the SINR is greater than the capture condition as follows

$$P_{Succ}(b) = \mathbb{P}[\gamma_i > b] = 1 - F_{\gamma_i}(b). \tag{17}$$

III. CAPACITY ANALYSIS

A. DERIVATION OF I_I

The distribution of the RV I_i is described by the scalar P_i^t and the RVs H_i, G_i, and Q_l. Given that H_i follows a Gamma distribution, then, $P_i^t H_i \sim \text{Gamma}(k_o, P_i^t\theta_o)$, $P_i^t > 0$, yielding

$$f_{\mathcal{H}_i}(h) = \frac{h^{k_o-1}e^{-\frac{h}{\vartheta}}}{\vartheta^{k_o}\Gamma(k_o)}, \tag{18}$$

where $\mathcal{H}_i = P_i^t H_i$ and $\vartheta = P_i^t\theta_o$. Assuming that $\mathcal{H}_i$ and Q_l are independent RVs, the product distribution $P_i = \mathcal{H}_i Q_l$ can then be used to obtain the PDF of P_i as follows

$$f_{P_i}(x) = \int_{-\infty}^{\infty} \frac{1}{|q|} f_{\mathcal{H}_i}(x/q) f_{Q_l}(q) dq, \tag{19}$$

which can be solved by substituting $f_{\mathcal{H}_i}(x/q)$ by (18) and $f_{Q_l}(q)$ by (13), yielding to

$$f_{P_i}(x) = \int_{R_{l+1}^{-\alpha}}^{R_l^{-\alpha}} -\frac{1}{|q|}\frac{(x/q)^{k_o-1}e^{\frac{-x}{q\vartheta}}}{\Gamma(k_o)\vartheta^{k_o}}\frac{2q^{\frac{-2}{\alpha}-1}}{\alpha(R_{l+1}^2 - R_l^2)}dq. \tag{20}$$

By solving the integral in (20) we obtain

$$f_{P_i}(x) = \left(\Gamma\left[k_o + \frac{2}{\alpha}, \frac{R_l^{\alpha}x}{\vartheta}\right] - \Gamma\left[k_o + \frac{2}{\alpha}, \frac{R_{l+1}^{\alpha}x}{\vartheta}\right]\right) \times \frac{2x^{-\frac{2+\alpha}{\alpha}}\vartheta^{\frac{2}{\alpha}}}{\alpha(R_{l+1}^2 - R_l^2)\Gamma(k_o)}. \tag{21}$$

The PDF of the RV I_i can be computed by the product distribution between the RVs P_i and G_i as follows

$$f_{I_i}(x) = \int_{-\infty}^{\infty} \frac{1}{|g|} f_{G_i}(g) f_{P_i}(x/g)\, dg. \tag{22}$$

For the rest of the analysis, we adopt three beam levels, i.e., $M = 3$, with one main lobe and two back lobes. Consequently, substituting $f_{G_i}(g)$ and $f_{P_i}(x/g)$ by (16) and (21), respectively, yields to

$$\begin{aligned} f_{I_i}(x) = {} & \frac{p_1^2}{G_1^2} f_{P_i}\left(\frac{x}{G_1^2}\right) + \frac{p_2^2}{G_2^2} f_{P_i}\left(\frac{x}{G_2^2}\right) + \frac{p_3^2}{G_3^2} f_{P_i}\left(\frac{x}{G_3^2}\right) \\ & + \frac{2p_1p_2}{G_1G_2} f_{P_i}\left(\frac{x}{G_1G_2}\right) + \frac{2p_1p_3}{G_1G_3} f_{P_i}\left(\frac{x}{G_1G_3}\right) \\ & + \frac{2p_2p_3}{G_2G_3} f_{P_i}\left(\frac{x}{G_2G_3}\right). \end{aligned} \tag{23}$$

As motioned before, the intended transmitter Tx_{i_o} is randomly selected from the set of $(n+1)$ nodes. Since the density of the nodes is not homogeneous across the interference area due to the mobility, the probability of selecting a node within the annulus l is given in (3). Therefore, the PDF of the intended received power, $P_{i_o}^r = P_i^t H_{i_o} G_{i_o} Q_l$, is given as follows

$$f_{P_{i_o}^r}(x) = \sum_{l=1}^{L} P_l f_{I_i}(x). \tag{24}$$

Therefore, the MGF of the interference seen at node Rx_o due to a single interferer, $M_{I_i}(s)$, is represented in (25), as shown at the bottom of the next page, where $\varrho(x) = {}_2\text{F}_1(k_o, \frac{-2}{\alpha}, \frac{-2+\alpha}{\alpha}, x)$.

B. DERIVATION OF I_L

Given that I_i's are independent, then for k active interferers, the MGF of the interference power I_l is the product between the MGFs of each I_i, given as follows

$$M_{I_l|k}(s) = M_{I_1}(s) \times M_{I_2}(s) \cdots \times M_{I_k}(s) = \left(M_{I_i}(s)\right)^k. \tag{26}$$

The distribution of the aggregate interference I_l can be then expressed as follows

$$f_{I_l}(j) = \sum_{k=0}^{n} f_{I_l}(j|X_l = k) P(X_l = k). \tag{27}$$

Based on (26), the MFG of I_l can be written as

$$\begin{aligned} \text{E}[e^{sI_l}] &= \sum_{k=0}^{n} P(X_l = k) \int_{-\infty}^{\infty} e^{sj} f_{I_l}(j|X_l = k)\, dj \\ &= \sum_{k=0}^{n} P(X_l = k) M_{I_l|k}(s). \end{aligned} \tag{28}$$

Using (2) and (26), we obtain

$$M_{I_l}(s) = \sum_{k=0}^{n} \frac{(\lambda_l A_l \tau_a M_{I_i}(s))^k}{k!} e^{-\lambda_l A_l \tau_a} = e^{\lambda_l A_l \tau_a (M_{I_i}(s)-1)}. \tag{29}$$

C. DERIVATION OF I_{AGG}

So far, we have derived the MGF of the interference caused to Rx_o by the interferers positioned within the annulus l. Using (6), the MGF of the total aggregate interference caused by interferers positioned in the L annuli can be written as follows

$$M_{I_{agg}}(s) = \prod_{l=1}^{L} M_{I_l}(s). \tag{30}$$

Substituting (29) in (30) leads to

$$M_{I_{agg}}(s) = e^{\left(\sum_{l=1}^{L} \lambda_l A_l \tau_a (M_{I_i}(s) - 1)\right)}. \tag{31}$$

For the approximation of I_{agg}, the moments can be obtained from (30) and then be matched with the respective moments of a given distribution.

D. DERIVATION OF Y

To determine the theoretical distributions that achieve the best accuracy in approximating the sample data, the simulated aggregate interference power plus noise is used to determine the parameters of different known distributions using the maximum log-likelihood estimation process. The different fit tests show that the GEV distribution exhibits a close

approximation of $Y = I_{agg} + P_{y_{res}} + \mathcal{N}$. This approximation will be explored and evaluated in the next steps of this work.

Admitting that Y follows the GEV distribution, then, the PDF of Y is given as follows

$$f_Y(y;\sigma,\gamma,\mu) \approx \frac{1}{\sigma} t(y)^{\gamma+1} e^{-t(y)}, \tag{32}$$

where

$$t(y) = \begin{cases} \left(1+\gamma(\frac{y-\mu}{\sigma})\right)^{-1/\gamma}, & \gamma \neq 0 \\ e^{-(y-\mu)/\sigma}, & \gamma = 0. \end{cases} \tag{33}$$

The symbols σ, γ, and μ are the GEV distribution parameters named the scale, shape, and location, respectively. The approximation in (32) requires to find the three GEV parameters σ, γ, and μ. Next, we use an efficient approach for computing the GEV parameters using the raw moments of Y.

The proposed approach uses the variance, skewness, and mean of the GEV distribution to set up three equations for σ, γ, and μ, as follows

$$\begin{cases} \mu'^{Y}_3 = sgn(\gamma) \\ \dfrac{\Gamma(1-3\gamma) - 3\Gamma(1-2\gamma)\Gamma(1-\gamma) + 2\Gamma(1-\gamma)^3}{\left(\Gamma(1-2\gamma) - \Gamma(1-\gamma)\right)^{3/2}}, \\ \qquad\qquad\qquad\qquad \gamma < \dfrac{1}{3} \\ \mu'^{Y}_2 = \dfrac{\sigma^2}{\gamma^2}\left(\Gamma(1-2\gamma) - \Gamma(1-\gamma)^2\right), \quad \gamma < \dfrac{1}{2} \\ \mu^Y_1 = \mu + \dfrac{\sigma}{\gamma}(\Gamma(1-\gamma)-1), \quad \gamma < 1, \end{cases} \tag{34}$$

where μ'^{Y}_3, μ'^{Y}_2, and μ^Y_1 are the skewness, variance, and mean of the GEV distribution, respectively. Note that the central moments (skewness and variance) can be written in terms of the raw-moments as follows

$$\begin{cases} \mu'^{Y}_3 = \dfrac{\mu^Y_3 - 3\mu^Y_1\left(\mu^Y_2 - (\mu^Y_1)^2\right) - (\mu^Y_1)^3}{\left(\mu^Y_2 - (\mu^Y_1)^2\right)^{3/2}} \\ \mu'^{Y}_2 = \mu^Y_2 - (\mu^Y_1)^2, \end{cases} \tag{35}$$

with

$$\begin{cases} \mu^Y_3 = \mu_3^{I_{agg}} + \mu_3^{P_{y_{res}}} + \mu_3^{\mathcal{N}} + 3\mu_2^{I_{agg}}\mu_1^{P_{y_{res}}} + 3\mu_1^{I_{agg}}\mu_2^{P_{y_{res}}} \\ +3\mu_2^{P_{y_{res}}}\mu_1^{\mathcal{N}} + 3\mu_1^{P_{y_{res}}}\mu_2^{\mathcal{N}} + 3\mu_2^{\mathcal{N}}\mu_1^{I_{agg}} + 3\mu_1^{\mathcal{N}}\mu_2^{I_{agg}} \\ +6\mu_1^{I_{agg}}\mu_1^{P_{y_{res}}}\mu_1^{\mathcal{N}} \\ \mu^Y_2 = \mu_2^{I_{agg}} + \mu_2^{P_{y_{res}}} + \mu_2^{\mathcal{N}} + 2\mu_1^{I_{agg}}\mu_1^{P_{y_{res}}} + 2\mu_1^{I_{agg}}\mu_1^{\mathcal{N}} \\ +2\mu_1^{P_{y_{res}}}\mu_1^{\mathcal{N}} \\ \mu^Y_1 = \mu_1^{I_{agg}} + \mu_1^{P_{y_{res}}} + \mu_1^{\mathcal{N}}. \end{cases} \tag{36}$$

The raw-moments of I_{agg}, denoted by $\mu_n^{I_{agg}}$, can be computed from (31), i.e., $\mu_n^{I_{agg}} = \frac{d^n}{ds^n} M_{I_{agg}}(s)|_{s=0}$. Besides, the raw-moments of $P_{y_{res}}$ are found using the PDF in (8), i.e., $\mu_n^{P_{y_{res}}} = \int_{-\infty}^{\infty} z^n f_{P_{y_{res}}}(z)dz$, as follows

$$\begin{cases} \mu_3^{P_{y_{res}}} = \dfrac{15\theta^3\sigma_x^6\Gamma(3+k)}{\Gamma(k)} \\ \mu_2^{P_{y_{res}}} = 3\,k(1+k)\theta^2\sigma_x^4 \\ \mu_1^{P_{y_{res}}} = k\theta\sigma_x^2. \end{cases} \tag{37}$$

Finally, the raw-moments of the RV $\mathcal{N} \sim$ Gamma $\left(\frac{1}{2}, 2\sigma_N^2\right)$ are as follows

$$\mu_3^{\mathcal{N}} = 15\sigma_N^6, \quad \mu_2^{\mathcal{N}} = 3\sigma_N^4, \quad \mu_1^{\mathcal{N}} = \sigma_N^2. \tag{38}$$

The first equation in (34) can be numerically solved using *MATHEMATICA* with the *FindRoot* command line or using *MATLAB* with the *vpasolve* command line in an efficient and straightforward manner to obtain γ. Subsequently, the parameters σ and μ are computed as follows

$$\begin{cases} \sigma = \sqrt{\dfrac{\gamma^2\mu'^{Y}_2}{\Gamma(1-2\gamma) - \Gamma(1-\gamma)^2}} \\ \mu = \mu^Y_1 - \dfrac{\sigma}{\gamma}(\Gamma(1-\gamma)-1). \end{cases} \tag{39}$$

E. COMPUTATION OF P_{SUCC}

Departing from (17) and given that $P^r_{i,o}$ and Y are independent RVs, P_{Succ} can be computed by solving the following expression

$$P_{Succ}(b) = 1 - \int_0^b \int_0^\infty y f_{P^r_{i_o}}(yz) f_Y(y) dy dz. \tag{40}$$

$$\begin{aligned} &M_{I_i}(s) \\ &= \frac{1}{(R_{l+1})^2 - (R_l)^2}\Big((R_{l+1})^2\Big(p_1^2\varrho\left(G_1^2(R_{l+1})^{-\alpha}\vartheta s\right) + p_2^2\varrho\left(G_2^2(R_{l+1})^{-\alpha}\vartheta s\right) + p_3^2\varrho\left(G_3^2(R_{l+1})^{-\alpha}\vartheta s\right) + 2\,p_1p_2 \\ &\times\varrho\left(G_1G_2(R_{l+1})^{-\alpha}\vartheta s\right) + 2\,p_1p_3\varrho\left(G_1G_3(R_{l+1})^{-\alpha}\vartheta s\right) + 2\,p_2p_3\varrho\left(G_2G_3(R_{l+1})^{-\alpha}\vartheta s\right)\Big) - (R_l)^2\Big(p_1^2\varrho\left(G_1^2(R_l)^{-\alpha}\vartheta s\right) + p_2^2 \\ &\times\varrho\left(G_2^2(R_l)^{-\alpha}\vartheta s\right) + p_3^2\varrho\left(G_3^2(R_l)^{-\alpha}\vartheta s\right) + 2\,p_1p_2\varrho\left(G_1G_2(R_l)^{-\alpha}\vartheta s\right) + 2\,p_1p_3\varrho\left(G_1G_3(R_l)^{-\alpha}\vartheta s\right) \\ &+ 2\,p_2p_3\varrho\left(G_2G_3(R_l)^{-\alpha}\vartheta s\right)\Big)\Big) \end{aligned} \tag{25}$$

Substituting $P^r_{i_o}$ and $f_Y(y)$ by (24) and (32), respectively, yields to

$$P_{Succ}(b) = 1 - \int_0^b \int_0^\infty \sum_{l=1}^{L} P_l \left(\frac{2y(yz)^{-\frac{2+\alpha}{\alpha}} \vartheta^{\frac{2}{\alpha}}}{\alpha(R_{l+1}^2 - R_l^2)\Gamma(k_o)} \times \left(\Gamma\left[k_o + \frac{2}{\alpha}, \frac{R_l^\alpha yz}{\vartheta}\right] - \Gamma\left[k_o + \frac{2}{\alpha}, \frac{R_{l+1}^\alpha yz}{\vartheta}\right] \right) \right) \times \frac{1}{\sigma} t(y)^{\gamma+1} e^{-t(y)} dy dz. \quad (41)$$

F. AVERAGE NUMBER OF SUCCESSFULLY RECEIVED PACKETS

Given that the N nodes are spatially i.i.d., then, the expected number of successfully received packets at node Rx_o can be approximated as follows

$$E_{RX}(b) \simeq \mathrm{E}[N] P_{Succ}(b) \simeq \sum_{l=1}^{L} \lambda_l A_l \tau_a P_{Succ}(b). \quad (42)$$

Note that (42) provides insights about the average number of successfully received packets taking into account the random number of interferers distributed within each annulus l. In other words, the model considers the average number of interferers between R_l and R_{L+1} given according to (2) when the maximum number of interferers is n. These interferers can also be seen as competing transmitters. However, it might be quite interesting to compute the average number of successfully received packets at Rx_o for a specific number of competing nodes $n = n^c$. Therefore, we define the RV N_s to represent the number of successfully received packets at the receiver Rx_o when n^c competing transmitters try to send information to node Rx_o. In Section IV, we present results of the PDF of N_s, represented by $f_{N_s}(n_s)$, depending on the accuracy level of residual SI estimation, mobility scenario, and detection threshold b, with $n_s \in \{1, \ldots, n^c\}$.

IV. PERFORMANCE ANALYSIS

The performance evaluation presented in this section is based on the comparison between the average number of successfully received packets derived theoretically in (42) with the one computed using the Monte Carlo simulation. The evaluation of the results considers the network scenario presented earlier in Fig. 1, the RWP model to describe the nodes' mobility, the IBFDX radio presented in Fig. 2 only at the receiver node, the M-beams model presented in Fig. 3 for directional beamforming communication, and the small-scale and large-scale fading described in Section II-E for the channel model. The network and mobility parameters are listed in Table 2. The nodes move according to the RWP mobility model during simulations lasting 3000 s in a square region of 1000 m × 1000 m. Three different values of nodes' pause time, T_p, are considered to define three different mobility scenarios. The beamforming model parameters are reported in Table 3. Finally, the IBFDX parameters adopted in the model presented in Section II are listed in Table 4. The parameters of the radio channel model also presented in Section II are provided in Table 5.

The number of transmitting nodes in each annulus of the circular model is sampled from the Poisson process defined in (2), with $n+1 = 100$ total nodes in the network. The RWP is considered to simulate the mobility of the nodes where the different T_p values are selected to define the average velocity of the nodes as described in Table 2, thus defining three different mobility scenarios, i.e., high velocity with $E[V] = 10.82$ m/s, intermediate velocity with $E[V] = 3.52$ m/s, and low velocity with $E[V] = 1.50$ m/s. The reference receiver Rx_o is positioned at $x_o = y_o = 500$ m. The nodes are distributed over a square simulation area of 1000 m ×1000 m and the nodes' mobility was sampled each second for 3000 s. The corresponding transmitter Tx_o is uniformly selected from the set of the 100 nodes to communicate with Rx_o, and the rest of the nodes act as interferers (or competitors trying to communicate to Rx_o). The analysis then considers the moving nodes located between R_1 and R_{L+1} m (achieved with $\rho = 10$ m and $L = 30$) as the competing nodes interested to transmit information to Rx_0.

TABLE 2. Network and mobility model parameters.

Symbol	Value
$n+1$	100 nodes
$\{X_{max}, Y_{max}\}$	{1000 m, 1000 m}
$\{x_o, y_o\}$	{500 m, 500 m}
$\{R_l, R_{L+1}\}$	{100 m, 400 m}
$\mathrm{E}[S]$	521.4 m
$\{V_{min}, V_{max}\}$	{5 m/s, 20 m/s}
$\{\rho, L\}$	{10 m, 30}
$\{\tau_a$, simulation time$\}$	{1, 3000 s}
Mobility scenarios	$\mathrm{E}[V]$ = 10.82 m/s for $T_p = 0$ $\mathrm{E}[V]$ = 3.52 m/s for T_p = 100 $\mathrm{E}[V]$ = 1.50 m/s for T_p = 300

In Fig. 4, we plot the successfully received packets, E_{RX}, versus the receiver threshold b, considering the three mobility scenarios identified in Table 2 in addition to the static case (without mobility $\mathrm{E}[V] = 0$ m/s) such as the one described in [23]. The matching between the theoretical and simulation curves validates the proposed modeling. In general, the results show an inverse relation between E_{RX} and b, meaning that more nodes can be decoded by decreasing the receiver threshold and they become limited by deciding on stringent threshold values. When comparing the results with respect to the mobility of the nodes, we observe two different behaviors based on the range of b values. The increase in mobility results in more decoded transmissions within the range of $b = -30$ dB and $b = -16$ dB. This indeed can be attributed to the increase of the average number of nodes in the vicinity of Rx_o for higher mobility scenarios, which is due to the properties of the RWP model. Compared with the mobility

TABLE 3. Beamforming model parameters.

Symbol	Value
$M = 1$	$G_1 = 0$ dB, $\omega_1 = 2\pi$
$M = 2$	$G_1 = 0$ dB, $G_2 = -7$ dB, $\omega_1 = \pi/3$, $\omega_2 = 5\pi/3$
$M = 3$	$G_1 = 0$ dB, $G_2 = -7$ dB, $G_3 = -10$, dB $\omega_1 = \pi/3$, $\omega_2 = 10\pi/9$, $\omega_3 = 5\pi/9$

TABLE 4. IBFDX model parameters.

Symbol	Value
σ_x^2	0.5
$\{K, \Omega\}$	{0 dB, 1 mW}
ϵ	{1.0, 0.8, 0.5}
ϕ	$\{0, \pi/4, \pi/2\}$

TABLE 5. Channel model parameters.

Symbol	Value
P_i^t	30 dBm
BW	180 kHz
$\mathcal{F}$	3 dB
$\{k_o, \theta_o\}$	{ 1, 1}

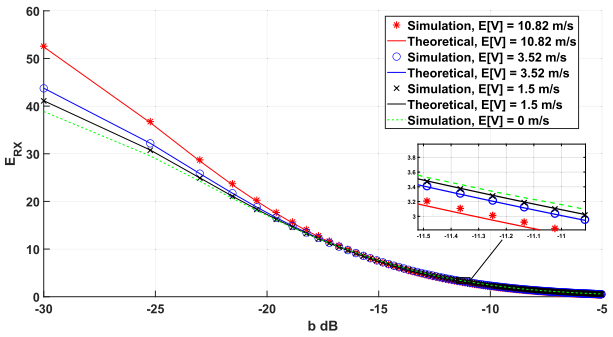

FIGURE 4. E_{RX} versus b for different mobility scenarios considering $M = 3$, $G_1 = 0$ dB, $G_2 = -7$ dB, $G_3 = -10$ dB, $\omega_1 = \pi/3$, $\omega_2 = 10\pi/9$, $\omega_3 = 5\pi/9$, $\epsilon = 1$, and $\phi = 0$.

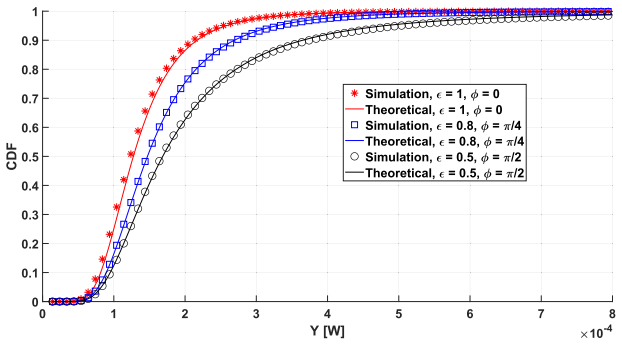

FIGURE 5. Total interference Y versus b for different levels of IBFDX estimation errors considering $M = 3$, $G_1 = 0$ dB, $G_2 = -7$ dB, $G_3 = -10$ dB, $\omega_1 = \pi/3$, $\omega_2 = 10\pi/9$, $\omega_3 = 5\pi/9$, and $E[V] = 10.82$ m/s.

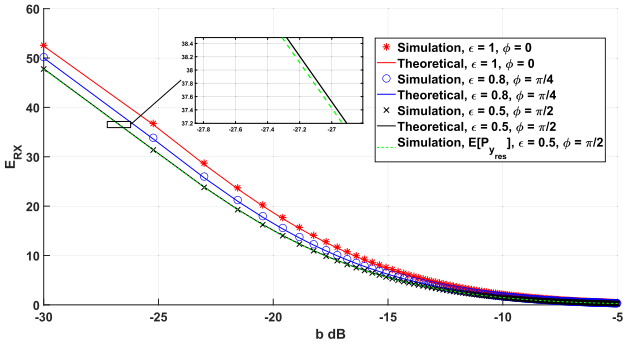

FIGURE 6. E_{RX} versus b for different levels of IBFDX estimation errors considering $M = 3$, $G_1 = 0$ dB, $G_2 = -7$ dB, $G_3 = -10$ dB, $\omega_1 = \pi/3$, $\omega_2 = 10\pi/9$, $\omega_3 = 5\pi/9$, and $E[V] = 10.82$ m/s.

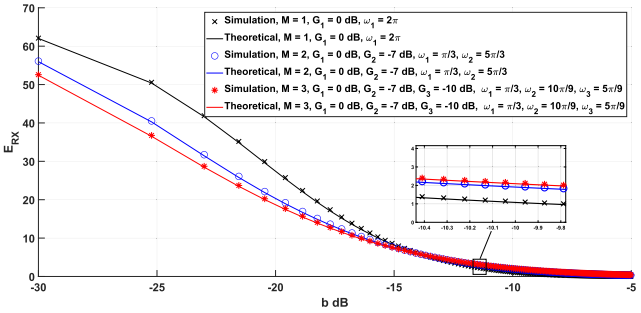

FIGURE 7. E_{RX} versus b for different M-beams considering $\epsilon = 1$, $\phi = 0$, and $E[V] = 10.82$ m/s.

cases, the number of decoded nodes is minimized over the range ($b = -30$ dB - $b = -16$ dB) in case of E$[V] = 0$ m/s.

This is due to the fact that the spatial distribution of the nodes is uniform when nodes are static, but as the average velocity of the nodes increases, a higher density of nodes is located at the center of the simulated region, i.e., close to the Rx_o node [25], leading to higher SINR values and more chance of successfully receiving more packets. On the other hand, the results indicate a different behavior when the range of the receiver threshold is higher, i.e., the range between $b = -16$ dB and $b = -5$ dB. Within this range, the number of successfully received nodes is maximized with no mobility. This is justified because the increase of b eliminates the chance of decoding packets with lower SINR values, and the gains on the SINR due to the increase in mobility can not be translated into an increase in the number of successfully received packets.

Next, we evaluate the influence of IBFDX estimation errors, particularly the gain error, $1 - \epsilon$, and phase estimation error, ϕ, on the interference and the number of decoded nodes. Initially, the total interference Y derived in Section III-D and given by (32) is evaluated in Fig. 5 for the three different levels of estimation errors reported in Table 4. The close matching between simulated curves and theoretical ones confirms the effectiveness of GEV distribution in approximating the total interference. The scenario with $\epsilon = 1.0$ and $\phi = 0$ represents the case of perfect estimation, i.e., $C = 0$, where the IBFDX radio can eliminate the SI

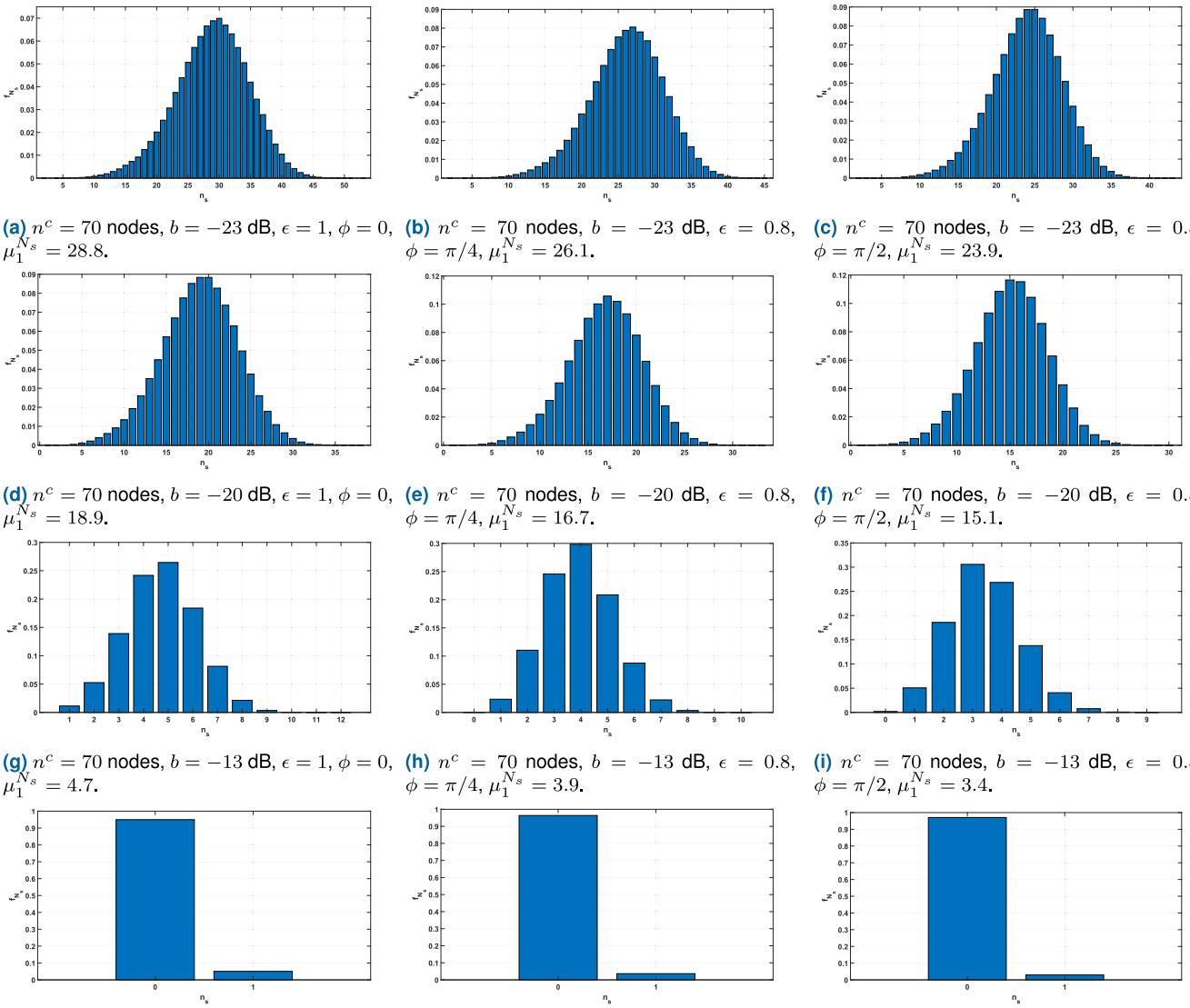

(a) $n^c = 70$ nodes, $b = -23$ dB, $\epsilon = 1$, $\phi = 0$, $\mu_1^{N_s} = 28.8$. (b) $n^c = 70$ nodes, $b = -23$ dB, $\epsilon = 0.8$, $\phi = \pi/4$, $\mu_1^{N_s} = 26.1$. (c) $n^c = 70$ nodes, $b = -23$ dB, $\epsilon = 0.5$, $\phi = \pi/2$, $\mu_1^{N_s} = 23.9$.

(d) $n^c = 70$ nodes, $b = -20$ dB, $\epsilon = 1$, $\phi = 0$, $\mu_1^{N_s} = 18.9$. (e) $n^c = 70$ nodes, $b = -20$ dB, $\epsilon = 0.8$, $\phi = \pi/4$, $\mu_1^{N_s} = 16.7$. (f) $n^c = 70$ nodes, $b = -20$ dB, $\epsilon = 0.5$, $\phi = \pi/2$, $\mu_1^{N_s} = 15.1$.

(g) $n^c = 70$ nodes, $b = -13$ dB, $\epsilon = 1$, $\phi = 0$, $\mu_1^{N_s} = 4.7$. (h) $n^c = 70$ nodes, $b = -13$ dB, $\epsilon = 0.8$, $\phi = \pi/4$, $\mu_1^{N_s} = 3.9$. (i) $n^c = 70$ nodes, $b = -13$ dB, $\epsilon = 0.5$, $\phi = \pi/2$, $\mu_1^{N_s} = 3.4$.

(j) $n^c = 70$ nodes, $b = 0$ dB, $\epsilon = 1$, $\phi = 0$, $\mu_1^{N_s} = 0.050$. (k) $n^c = 70$ nodes, $b = 0$ dB, $\epsilon = 0.8$, $\phi = \pi/4$, $\mu_1^{N_s} = 0.036$. (l) $n^c = 70$ nodes, $b = 0$ dB, $\epsilon = 0.5$, $\phi = \pi/2$, $\mu_1^{N_s} = 0.029$.

FIGURE 8. The computation of $f_{N_S}(n_s)$ for different levels of IBFDX estimation errors considering $M = 3$, $G_1 = 0$ dB, $G_2 = -7$ dB, $G_3 = -10$ dB, $\omega_1 = \pi/3$, $\omega_2 = 10\pi/9$, $\omega_3 = 5\pi/9$, and $E[V] = 10.82$ m/s.

totally, resulting in the lowest values of Y. With $\epsilon = 0.8$ and $\phi = \pi/4$ we obtain $C = 0.5$, thus, an extra residual SI is added to the aggregate interference and noise, resulting in a degraded performance compared with the perfect estimation case. The last case represents the worst considered estimation scenario with $\epsilon = 0.5$ and $\phi = \pi/2$, leading to $C = 1.25$, where the receiver experiences a higher residual SI level and consequently higher Y values.

To highlight the effect of Y on E_{RX}, Fig. 6 illustrates E_{RX} versus b for the same SI estimation scenarios considered in Fig. 5. The perfect estimation scenario achieves the best results in terms of the number of successfully received packets due to the lowest induced interference. As expected, with $\epsilon = 0.8$ and $\phi = \pi/4$, the number of decoded nodes is degraded when compared with the perfect estimation case. In the worst estimation scenario with $\epsilon = 0.5$ and $\phi = \pi/2$, the receiver experiences a higher residual SI level and, consequently, fewer nodes can be successfully received by Rx_o. The results show that the capability of the IBFDX

TABLE 6. The successfully received packets, n_s, achieved when considering the first, second, and third quartiles of the results illustrated in Fig. 8.

	$Q_1(0\% - 25\%)$	$Q_2(25\% - 50\%)$	$Q_3(50\% - 75\%)$
Fig. 8a	$n_s = 23$ packets	$n_s = 27$ packets	$n_s = 31$ packets
Fig. 8b	$n_s = 21$ packets	$n_s = 24$ packets	$n_s = 28$ packets
Fig. 8c	$n_s = 19$ packets	$n_s = 22$ packets	$n_s = 25$ packets
Fig. 8d	$n_s = 15$ packets	$n_s = 18$ packets	$n_s = 21$ packets
Fig. 8e	$n_s = 13$ packets	$n_s = 16$ packets	$n_s = 18$ packets
Fig. 8f	$n_s = 12$ packets	$n_s = 14$ packets	$n_s = 16$ packets
Fig. 8g	$n_s = 3$ packets	$n_s = 4$ packets	$n_s = 5$ packets
Fig. 8h	$n_s = 3$ packets	$n_s = 4$ packets	$n_s = 5$ packets
Fig. 8i	$n_s = 3$ packets	$n_s = 3$ packets	$n_s = 4$ packets

TABLE 7. Probability density of the number of successfully received packets, $f_{N_S}(n_S)$, for different levels of IBFDX estimation errors considering $n^c = 70$ nodes and $b = -20$ dB.

n_s	$\epsilon = 1, \phi = 0$	$\epsilon = 0.8, \phi = \pi/4$	$\epsilon = 0.5, \phi = \pi/2$
1	0.0000	0.0000	0.0000
2	0.0000	0.0000	0.0001
3	0.0001	0.0002	0.0004
4	0.0004	0.0007	0.0010
5	0.0011	0.0015	0.0022
6	0.0022	0.0032	0.0047
7	0.0040	0.0058	0.0087
8	0.0062	0.0094	0.0149
9	0.0092	0.0146	0.0240
10	0.0134	0.0220	0.0363
11	0.0193	0.0318	0.0529
12	0.0260	0.0442	0.0732
13	0.0351	0.0598	0.0933
14	0.0450	0.0744	0.1085
15	0.0571	0.0900	0.1165
16	0.0670	0.1002	0.1153
17	0.0775	0.1058	0.1043
18	0.0852	0.1020	0.0859
19	0.0883	0.0932	0.0629
20	0.0883	0.0781	0.0426
21	0.0827	0.0595	0.0263
22	0.0737	0.0424	0.0140
23	0.0629	0.0280	0.0075
24	0.0496	0.0162	0.0031
25	0.0375	0.0088	0.0015
26	0.0261	0.0047	0.0004
27	0.0178	0.0020	0.0001
28	0.0109	0.0008	0.0000
29	0.0065	0.0003	0.0000
30	0.0036	0.0001	0.0000
31	0.0017	0.0000	0.0000
32	0.0007	0.0000	0.0000
33	0.0003	0.0000	0.0000
34	0.0002	0.0000	0.0000
35	0.0001	0.0000	0.0000
36	0.0000	0.0000	0.0000
37	0.0000	0.0000	0.0000
38	0.0000	0.0000	0.0000

system to eliminate the residual SI is of high importance for lower b values, but its impact is reduced as b increases and the number of successfully received packets converges to 0. Finally, similar with the approach presented in [24], where the average of the SI is considered instead of probabilistic distribution, we have simulated E_{RX} considering the average SI $\left(\mathrm{E}[P_{y_{res}}]\right)$ with $\epsilon = 0.5$ and $\phi = \pi/2$. As can be seen, the results considering the average SI are similar when compared to the SI originated using probabilistic modeling, meaning that while the assumption of the distribution leads to a more accurate model the assumption of the average self-interference model is also a good approximation for some gain and phase estimation error values.

The results in Fig. 7 validate the proposed beamforming model. With low b values, the received SINR from the different nodes is more likely to be greater than the threshold b. For lower values of b, as for $b = -30$ dB, the average number of received packets can benefit from the omnidirectional transmission, as in the case of isotropic transmission (achieved with $G_1 = 0$ dB over $\omega_1 = 2\pi$), because more nodes can reach Rx_o with SINR values greater than the threshold b. However, this is an extreme case when b value is really too low, which is unrealistic for practical systems. For higher b values only nodes with high SINR values can be decoded. For b values around -10 dB, we observe that directional antennas are advantageous. In this region, E_{RX} increases by introducing more side-lobes, i.e., E_{RX} is higher with $M = 3$ compared to $M = 2$, since the adoption of higher M limits the interference radiation overall the angular space and instead, direct the radiation beam toward a specific direction improve the overall performance.

As a final contribution, in Fig. 8 we compute the PDF of the number of successfully received packets, $f_{N_s}(n_s)$, for a specific number of simultaneously interfering nodes n^c in which ($n^c \leq n$). The average number of successfully received packets is indicated in the caption of each figure by the symbol $\mu_1^{N_s}$. We aim at identifying the achievable number of successfully received packets, n_s, based on different IBFDX estimation errors and considering various receiver threshold values b. These results are of interest for regulating the access of multiple transmitters to a single receiver, highlighting the importance of proper scheduling in exploiting the benefits offered by the adoption of IBFDX radios. As can be seen, although the number of competing nodes, $n^c = 70$, is maintained, the shape of the distribution of the number of successfully received packets is significantly changed for the considered scenarios.

Fig. 8a, Fig. 8b, and Fig. 8c consider the computation of $f_{N_s}(n_s)$ over different IBFDX estimation error scenarios with $b = -23$ dB. The first quartile Q_1 (0%-25% of the total observations), the second quartile Q_2 (25%-50% of the total observations), and the third quartile Q_3 (50%-75% of the total observations) of each figure are reported in Table 6. Considering Q_1, Q_2, and Q_3 of Fig. 8a, we observe that $n_s = 23$ nodes, $n_s = 27$ nodes, and $n_s = 31$ nodes, can be successfully received by Rx_o, respectively, with ($\epsilon = 1, \phi = 0$), when $n^c = 70$ nodes compete to transmit for Rx_o. Taking Q_1 as an example, the number of successfully received packets, n_s, decreases as the quality of the SI channel estimation decreases and, in this case, the 23 successfully received packets in the optimal SI channel estimation case decrease to $n_s = 21$ and $n_s = 19$ when moderate quality SI channel estimation ($\epsilon = 0.8, \phi = \pi/4$) and low quality SI channel estimation ($\epsilon = 0.5, \phi = \pi/2$) occur, respectively.

The results in Fig. 8d, Fig. 8e, and Fig. 8f are for $b = -20$ dB, while Fig. 8g, Fig. 8h, and Fig. 8i are for $b = -13$ dB. As b decreases the number of successfully received packets increases although the distribution always results in an asymmetrical one. Finally, Fig. 8j, Fig. 8k, and Fig. 8l represent the case of an SPR receiver, showing that for such high levels of interference, SPR receivers are not adequate,

as the probability of successfully receive a single packet is close to 0. The values of the discrete distributions in Fig. 8 are provided in the Appendix to support further work in the area.

V. CONCLUSION

In this paper, we have presented a characterization of the capacity of directional IBFDX mobile wireless networks. We evaluated the impact of nodes' mobility, directive beams, and full-duplex capabilities on the network capacity. We derived the signal-to-interference-plus-noise ratio (SINR) for a reference receiver, considering the combined effects of mobility, directive beams, and full-duplex communications. The derived SINR was the basis to compute the network's capacity, measured in terms of the average number of successfully received packets by a single receiver. Extensive simulations were performed to validate the proposed model, characterizing the various scenarios of mobility levels, self-interference suppression levels in the full-duplex wireless system, and different receiving thresholds. The simulation results confirmed the accuracy and effectiveness of the derived SINR-based capacity characterization model under real-world conditions.

The paper results show that the specific features of the RWP mobility model show that an increase in the mobility level of the nodes is advantageous, as it increases the SINR of the transmitting nodes located in the vicinity of the receiver. The suppression of the residual SI also plays a vital role in the receiver's performance, as expected. Lower values of residual SI increase the probability of successfully receiving more packets, as shown in the presented results. Finally, we showed that for a practical receiving threshold range (b), the adoption of directional antennas is advantageous, as the SINR can be significantly increased due to the adoption of directive antennas. However, omnidirectional communications can also be beneficial if the receiver's threshold b can be lowered, which is currently impractical due to the multiple impairments of the existing receivers, although theoretically shown in our results.

A. MODEL APPLICATIONS

The proposed model considered an uplink scenario where a massive number of transmitters adopt directional communications. The receiver is equipped with a self-interference canceller meaning that it can also transmit while receiving. Given that the model is based on an SINR threshold and not on a specific detection scheme, it is generic enough to represent multiple practical examples, including but not limited to:

- Evolved NB-IoT network operation: in NB-IoT cellular operational scenarios, multiple nodes transmit data to a single node, usually a base station or a small cell. The proposed model can be used for that purpose and might consider an evolved version of NB-IoT, where the transmitters can adopt directional communications, and the small cell can simultaneously receive and transmit to a macro-cell or simply use the band to also transmit in the downlink direction using in-band full-duplex communications;
- Ultra-dense scenarios of massive connectivity: where the threshold-based SINR decoders can mimic the coded-based communication systems, e.g., LoRa devices - by properly changing the b value according to the adopted codes, the transmitters may or may not adopt directional beamforming, and the receiving gateway can benefit from in-band full-duplex to relay information in a multi-hop operation. In this case, the medium access probability can be a variable to maximize the performance of the network supported by the proposed model.

B. FUTURE WORK

The model proposed in this work can be extended in multiple directions. The assumption of a single antenna at the receiver represents a lower-bound performance. However, it would be interesting to extend the proposed model for the scenario when the receivers are equipped with multiple antennas to quantify its performance gain. Another direction is the characterization of the performance of beyond 5G network scenarios. In this case, we highlight the Grant-free NOMA (GF-NOMA) concept, which is being proposed for 6G networks. The study of GF-NOMA uplink networks can also be studied in the power domain, particularly for code-domain systems. The proposed model can be easily extended to consider code-domain GF-NOMA, where orthogonal sequences, such as Zadoff-Chu sequences, can be easily integrated to study the performance of grant-free networks that avoid random access requests to perform radio resources' reservation and thus increase the network scalability.

APPENDIX

NUMERICAL RESULTS OF $F_{N_S}(N_S)$

The numerical results in Table 7 represent the density values, $f_{N_s}(n_s)$, shown in Figs. 8a, 8b, and 8c.

REFERENCES

[1] P. Zhou, X. Wang, and R. Rao, "Asymptotic capacity of infrastructure wireless mesh networks," *IEEE Trans. Mobile Comput.*, vol. 7, no. 8, pp. 1011–1024, Aug. 2008.
[2] G. Farhadi and N. Beaulieu, "On the ergodic capacity of wireless relaying systems over Rayleigh fading channels," *IEEE Trans. Wireless Commun.*, vol. 7, no. 11, pp. 4462–4467, Nov. 2008.
[3] M.-F. Guo, X. Wang, and M.-Y. Wu, "On the capacity of k-MPR wireless networks," *IEEE Trans. Wireless Commun.*, vol. 8, no. 7, pp. 3878–3886, Jul. 2009.
[4] Y. Jaradat, H. Huang, M. Masoud, and I. Janoud, "Capacity of wireless networks with directed energy links in the presence of obstacles," *IEEE Trans. Wireless Commun.*, vol. 16, no. 8, pp. 5273–5283, Aug. 2017.
[5] X. Tong, B. Chang, Z. Meng, G. Zhao, and Z. Chen, "Calculating terahertz channel capacity under beam misalignment and user mobility," *IEEE Wireless Commun. Lett.*, vol. 11, no. 2, pp. 348–351, Feb. 2022.
[6] X. Ma, D. Zhang, M. Xiao, C. Huang, and Z. Chen, "Cooperative beamforming for RIS-aided cell-free massive MIMO networks," *IEEE Trans. Wireless Commun.*, vol. 22, no. 11, pp. 7243–7258, Nov. 2023.
[7] R. Ramanathan, J. Redi, C. Santivanez, D. Wiggins, and S. Polit, "Ad hoc networking with directional antennas: A complete system solution," *IEEE J. Sel. Areas Commun.*, vol. 23, no. 3, pp. 496–506, Mar. 2005.

[8] N. Chukhno, O. Chukhno, D. Moltchanov, A. Molinaro, Y. Gaidamaka, K. Samouylov, Y. Koucheryavy, and G. Araniti, "Optimal multicasting in millimeter wave 5G NR with multi-beam directional antennas," *IEEE Trans. Mobile Comput.*, vol. 22, no. 6, pp. 3572–3588, Jun. 2023.

[9] F. Fredj, Y. Al-Eryani, S. Maghsudi, M. Akrout, and E. Hossain, "Distributed beamforming techniques for cell-free wireless networks using deep reinforcement learning," *IEEE Trans. Cognit. Commun. Netw.*, vol. 8, no. 2, pp. 1186–1201, Jun. 2022.

[10] K. Maruta and C.-J. Ahn, "Uplink interference suppression by semi-blind adaptive array with decision feedback channel estimation on multicell massive MIMO systems," *IEEE Trans. Commun.*, vol. 66, no. 12, pp. 6123–6134, Dec. 2018.

[11] Y. J. Kim and Y. S. Cho, "Beam-tracking technique for millimeter-wave cellular systems using subarray structures," *IEEE Trans. Veh. Technol.*, vol. 67, no. 8, pp. 7806–7810, Aug. 2018.

[12] H. Thomsen, P. Popovski, E. D. Carvalho, N. K. Pratas, D. M. Kim, and F. Boccardi, "CoMPflex: CoMP for in-band wireless full duplex," *IEEE Wireless Commun. Lett.*, vol. 5, no. 2, pp. 144–147, Apr. 2016.

[13] S. Haddad, A. Özgür, and E. Telatar, "Can full-duplex more than double the capacity of wireless networks?" in *Proc. IEEE Int. Symp. Inf. Theory (ISIT)*, Jun. 2017, pp. 963–967.

[14] E. Everett, A. Sahai, and A. Sabharwal, "Passive self-interference suppression for full-duplex infrastructure nodes," *IEEE Trans. Wireless Commun.*, vol. 13, no. 2, pp. 680–694, Feb. 2014.

[15] E. Ahmed, A. M. Eltawil, Z. Li, and B. A. Cetiner, "Full-duplex systems using multireconfigurable antennas," *IEEE Trans. Wireless Commun.*, vol. 14, no. 11, pp. 5971–5983, Nov. 2015.

[16] X. Huang, A. Tuyen Le, and Y. J. Guo, "ALMS loop analyses with higher-order statistics and strategies for joint analog and digital self-interference cancellation," *IEEE Trans. Wireless Commun.*, vol. 20, no. 10, pp. 6467–6480, Oct. 2021.

[17] A. T. Le, X. Huang, L. C. Tran, and Y. J. Guo, "On the impacts of I/Q imbalance in analog least mean square adaptive filter for self-interference cancellation in full-duplex radios," *IEEE Trans. Veh. Technol.*, vol. 71, no. 10, pp. 10683–10693, Oct. 2022.

[18] Y. He, X. Yin, and H. Chen, "Spatiotemporal characterization of self-interference channels for 60-GHz full-duplex communication," *IEEE Antennas Wireless Propag. Lett.*, vol. 16, pp. 2220–2223, 2017.

[19] L. Irio and R. Oliveira, "Distribution of the residual self-interference power in in-band full-duplex wireless systems," *IEEE Access*, vol. 7, pp. 57516–57526, 2019.

[20] E. Everett, M. Duarte, C. Dick, and A. Sabharwal, "Empowering full-duplex wireless communication by exploiting directional diversity," in *Proc. 45th Asilomar Conf. Signals, Syst. Comput. (ASILOMAR)*, Nov. 2011, pp. 2002–2006.

[21] C. Psomas, C. Skouroumounis, I. Krikidis, A. Kalis, Z. Theodosiou, and A. Kounoudes, "Performance gains from directional antennas in full-duplex systems," in *Proc. IEEE Int. Conf. Microw., Commun., Antennas Electron. Syst. (COMCAS)*, Nov. 2015, pp. 1–5.

[22] G. Y. Suk, S.-M. Kim, J. Kwak, S. Hur, E. Kim, and C.-B. Chae, "Full duplex integrated access and backhaul for 5G NR: Analyses and prototype measurements," *IEEE Wireless Commun.*, vol. 29, no. 4, pp. 40–46, Aug. 2022.

[23] C. Psomas, M. Mohammadi, I. Krikidis, and H. A. Suraweera, "Impact of directionality on interference mitigation in full-duplex cellular networks," *IEEE Trans. Wireless Commun.*, vol. 16, no. 1, pp. 487–502, Jan. 2017.

[24] D. Qin and Z. Ding, "Transport capacity analysis of wireless in-band full duplex ad hoc networks," *IEEE Trans. Commun.*, vol. 65, no. 3, pp. 1303–1318, Mar. 2017.

[25] C. Bettstetter, G. Resta, and P. Santi, "The node distribution of the random waypoint mobility model for wireless ad hoc networks," *IEEE Trans. Mobile Comput.*, vol. 2, no. 3, pp. 257–269, Jul. 2003.

[26] L. Irio, R. Oliveira, and L. Bernardo, "Aggregate interference in random waypoint mobile networks," *IEEE Commun. Lett.*, vol. 19, no. 6, pp. 1021–1024, Jun. 2015.

[27] L. Irio, A. Furtado, R. Oliveira, L. Bernardo, and R. Dinis, "Interference characterization in random waypoint mobile networks," *IEEE Trans. Wireless Commun.*, vol. 17, no. 11, pp. 7340–7351, Nov. 2018.

[28] A. Papoulis and S. U. Pillai, *Probability Random Variables and Stochastic Processes*, 4th ed. New York, NY, USA: McGraw-Hill, 2001.

[29] M. Haenggi and R. K. Ganti, "Interference in large wireless networks," *Found. Trends Netw.*, vol. 3, no. 2, pp. 127–248, 2009.

[30] X. Huang, A. Tuyen Le, and Y. J. Guo, "Joint analog and digital self-interference cancellation for full duplex transceiver with frequency-dependent I/Q imbalance," *IEEE Trans. Wireless Commun.*, vol. 22, no. 4, pp. 2364–2378, Apr. 2023.

[31] A. T. Abusabah, L. Irio, R. Oliveira, and D. B. da Costa, "Approximate distributions of the residual self-interference power in multi-tap full-duplex systems," *IEEE Wireless Commun. Lett.*, vol. 10, no. 4, pp. 755–759, Apr. 2021.

[32] T. Bai and R. W. Heath, "Coverage and rate analysis for millimeter-wave cellular networks," *IEEE Trans. Wireless Commun.*, vol. 14, no. 2, pp. 1100–1114, Feb. 2015.

[33] S. Singh, M. N. Kulkarni, A. Ghosh, and J. G. Andrews, "Tractable model for rate in self-backhauled millimeter wave cellular networks," *IEEE J. Sel. Areas Commun.*, vol. 33, no. 10, pp. 2196–2211, Oct. 2015.

[34] M. Di Renzo, "Stochastic geometry modeling and analysis of multi-tier millimeter wave cellular networks," *IEEE Trans. Wireless Commun.*, vol. 14, no. 9, pp. 5038–5057, Sep. 2015.

[35] J. Wildman, P. H. J. Nardelli, M. Latva-aho, and S. Weber, "On the joint impact of beamwidth and orientation error on throughput in directional wireless Poisson networks," *IEEE Trans. Wireless Commun.*, vol. 13, no. 12, pp. 7072–7085, Dec. 2014.

[36] G. D. Nguyen, A. Ephremides, and J. E. Wieselthier, "On capture in random-access systems," in *Proc. IEEE Int. Symp. Inf. Theory*, Jul. 2006, pp. 2072–2076.

[37] B. Hajek, A. Krishna, and R. O. LaMaire, "On the capture probability for a large number of stations," *IEEE Trans. Commun.*, vol. 45, no. 2, pp. 254–260, Feb. 1997.

AYMAN T. ABUSABAH (Member, IEEE) received the B.S. degree in telecommunication engineering from Yarmouk University, Irbid, Jordan, and the M.S. degree in telecommunication engineering from Medipol University, Istanbul, Turkey. He is currently pursuing the Ph.D. degree in Telecommunication Engineering with the Faculdade de Ciências e Tecnologia (FCT), Universidade Nova de Lisboa, Portugal. During the Ph.D. study, he joined the TeamUp5G [a European Training Network (ETN)] project as an Early Stage Researcher (ESR). He benefited from a unique doctoral training programme covering scientific, technical, business aspects, and spent time experimenting the research in real scenarios. His research interests include the design of PHY/MAC architectures for WLANs and future 5G/6G mobile networks.

RODOLFO OLIVEIRA (Senior Member, IEEE) received the Licenciatura degree in electrical engineering from the Faculdade de Ciências e Tecnologia (FCT), Universidade Nova de Lisboa (UNL), Lisbon, Portugal, in 2000, the M.Sc. degree in electrical and computer engineering from the Instituto Superior Técnico, Technical University of Lisbon, in 2003, and the Ph.D. degree in electrical engineering from UNL, in 2009. From 2007 to 2008, he was a Visiting Researcher with the University of Thessaly. From 2011 to 2012, he was a Visiting Scholar with Carnegie Mellon University. He is currently with the Department of Electrical and Computer Engineering, UNL. He is also a Senior Researcher with the Instituto de Telecomunicações. His research interests include wireless communications, computer networks, and computer science. He serves on the editorial board of *Ad Hoc Networks* (Elsevier), *ITU Journal on Future and Evolving Technologies* (ITU J-FET), IEEE Open Journal of the Communications Society, and IEEE Communications Letters.